magnetochemistry

MDPI

Article

Photothermal Hyperthermia Study of Ag/Ni and Ag/Fe Plasmonic Particles Synthesized Using Dual-Pulsed Laser

Imran Ali [1], Jun Chen [2], Saeed Ahmed Khan [3], Yasir Jamil [4], Aqeel Ahmed Shah [5], Abdul Karim Shah [6], Sadaf Jamal Gilani [7], May Nasser Bin Jumah [8,9,10], Yusra Fazal [1], Yunxiang Pan [1,*] and Zhonghua Shen [1,*]

1 School of Science, Nanjing University of Science and Technology, Nanjing 210094, China
2 Institute of Optoelectronics Nanomaterials, MIIT Key Laboratory of Advanced Display Materials and Devices, College of Materials Science and Engineering, Nanjing University of Science and Technology, Nanjing 210094, China
3 Department of Electrical Engineering, Sukkur IBA University, Sukkur 65200, Pakistan
4 Laser Spectroscopy Lab, Department of Physics, University of Agriculture, Faisalabad 38000, Pakistan
5 Wet Chemistry Laboratory, Department of Metallurgical Engineering, NED University of Engineering and Technology, University Road, Karachi 75270, Pakistan
6 Department of Chemical Engineering, Dawood University of Engineering and Technology, Karachi 75270, Pakistan
7 Department of Basic Health Sciences, Foundation Year of Health Colleges, Princess Nourah Bint Abdulrahman University, Riyadh 11671, Saudi Arabia
8 Biology Department, College of Science, Princess Nourah Bint Abdulrahman University, Riyadh 11671, Saudi Arabia
9 Environment and Biomaterial Unit, Health Sciences Research Center, Princess Nourah Bint Abdulrahman University, Riyadh 11671, Saudi Arabia
10 Saudi Society for Applied Science, Princess Nourah Bint Abdulrahman University, Riyadh 11671, Saudi Arabia
* Correspondence: yunxiangpan@njust.edu.cn (Y.P.); shenzh@njust.edu.cn (Z.S.)

Citation: Ali, I.; Chen, J.; Ahmed Khan, S.; Jamil, Y.; Shah, A.A.; Shah, A.K.; Gilani, S.J.; Bin Jumah, M.N.; Fazal, Y.; Pan, Y.; et al. Photothermal Hyperthermia Study of Ag/Ni and Ag/Fe Plasmonic Particles Synthesized Using Dual-Pulsed Laser. *Magnetochemistry* **2023**, *9*, 59. https://doi.org/10.3390/magnetochemistry9030059

Academic Editors: Mohan Chandra Mathpal, Promod Kumar, Jai Prakash and Vinod Kumar

Received: 13 January 2023
Revised: 13 February 2023
Accepted: 16 February 2023
Published: 22 February 2023

Abstract: Magneto-plasmonic Ag/Ni and Ag/Fe nanoparticles (NPs) were synthesized in this work using the environmentally safe and contaminant-free dual-pulsed Q-switched Nd:YAG 1064 nm laser ablation method. The optical and magnetic characteristics of synthesized nanomaterials were investigated using a vibrating sample magnetometer and an ultraviolet-visible absorption spectrometer. According to transmission electron microscopy (TEM), the shape of Ag/Ni and Ag/Fe NPs seems to be spherical, with mean diameters of 7.3 nm and 11.5 nm, respectively. X-ray diffraction (XRD) was used in order to investigate and describe the phase structures of the synthesized nanomaterials. The synthesized NPs reached maximum temperatures such as 48.9, 60, 63.4, 70, 75, and 79 °C for Ag/Ni nanofluid and 52, 56, 60, 68, 71, and 72 °C for Ag/Fe nanofluid when these nanofluids were subjected to an NIR 808 nm laser with operating powers of 1.24, 1.76, 2.36, 2.91, 3.5, and 4 W, respectively. Because of the plasmonic hyperthermia properties of nanoparticles, nanofluids display higher temperature profiles than pure water. According to these findings, plasmonic nanoparticles based on silver might be used to treat hyperthermia.

Keywords: double-pulsed laser ablation; plasmonic nanomaterials; photothermal hyperthermia

1. Introduction

Nanoscale studies of silver and gold have been explored for several applications due to their plasmonic properties, including photocatalysis [1], photoluminescence imaging [2], sensor [3], photothermal hyperthermia [4], and potential viricidal material for personal protective equipment [5]. Furthermore, they might also be utilized in other areas, such as liquid crystals, as a dopant in order to change the optical (linear/non-linear), dielectric, and electro-optical properties of the liquid crystals [6]. Because of their high surface-to-volume ratio [7], electrodynamic interactions [8], and quantum effects [9], nanoparticles formed from these materials exhibit very different characteristics than their bulk counterparts as a

consequence of their light-matter interactions. These features cause free electrons on the metal surface to collectively oscillate throughout the particle's entire volume, resulting in localized surface plasmon resonance (LSPR) [10]. In photothermal treatment [11], a light source is used to stimulate photothermal therapy agents, causing them to release energy in the form of heat. Photothermal agents often use organic dyes [12], which might prevent issues including photostability and photobleaching [13,14]. Ohmic heating [15], whole-body hyperthermia [16], and microwave systems [17] may all raise tumor temperatures. One drawback shared by all approaches is that it is difficult to regulate the localized amount of heat applied to tumor tissue in order to achieve the optimal therapeutic temperature.

However, unlike conventional composites, the heat generated by hybrid composites is concentrated precisely where it is needed. When combined with laser light and external magnetic fields, these hybrid NPs might be employed for photothermal treatment and targeted hyperthermia [18]. When using plasmonic composites, the hyperthermia they generate might be precisely directed to a specific area. Further, they decrease the intensity of the irradiated laser and the concentration of the NPs needed to achieve the same results [19]. Nanomaterials' generated heat is relied on for the direct, non-contact irradiation of the sample with light using a spectrum of wavelengths ranging from 650 to 1350 nm, which is safe for the tissues that are being irradiated [20,21]. Several studies have shown great potential for using magnetic nanoparticles containing iron oxide in photothermal therapies [22–24], via activation with near infrared irradiation. A near-infrared (808 nm) laser has been used to study the photothermal response of $Mn_{1-x}Ni_xFe_2O_4$ [25].

Recently, gold-shelled iron oxide coated with polyethylene glycol nanoparticles has been used to enhance photothermal ablation. In addition to silver's significant anti-inflammatory, antibacterial, and antifungal activities, silver-based nanoparticles are also a potential candidate for photothermal agents [26–28]. The chemical synthesis of Ag/Ni composites with antioxidation, magnetic, and optical characteristics [29] and Ag/Ni nanoparticles for the catalytic generation of hydrogen [30] using a one-pot seed growing process have previously been described. Lower cytotoxicity of hybrid magnetite-Ag nanomaterials and a greatly increased magnetic hyperthermia effect of Ag/Fe bimetallic NPs were observed [31]. Thermochemical breakdown [30], pulsed electrodeposition [32], the seed-induced heterogeneous nucleation method [33], the liquid-phase reduction method [34], and chemical procedures [35] are few of the methods published for synthesizing magneto-plasmonic hybrid composites. While there are benefits to using these methods, there are also potential drawbacks, including contamination, lengthy processing times, NPs existing in the solid phase, the need for numerous purifications, and a complex synthesis approach [33]. Laser-assisted synthesis of NPs has emerged as an alternative synthesis method for hybrid composites generation due to its contamination-free, rapid, environmentally friendly nature, simple experimental setup, reduced or eliminated purification needs, and synthesis without involving chemical or toxic precursors, all of which are highly promising for biological applications [36–39]. Laser-assisted synthesis of magneto-plasmonic hybrid composites, such as Fe-doped Ag nanomaterials, was reported for photothermal application [40]. Previous research [41] created bimetallic Fe_3O_4/Ag nanoparticles by performing a two-step laser ablation in pure water. This work is an extension of previously published research [4] that examined the photothermal response of an Ag/Co nanofluid generated using a dual-pulsed laser ablation approach.

A simple and contamination-free technique for synthesizing magneto-plasmonic nanostructures by making use of a double Nd:YAG laser pulse has been reported. There have been no reports about the fabrication of Ag/Ni and Ag/Fe nanomaterials using dual-pulsed laser ablation techniques for the study of laser hyperthermia, such as the increase in nanofluid temperature as a function of NIR 808 nm laser power. The present work deals with the photothermal response study of bimetallic nanoparticles with optimization of the synthesis conditions of these bimetallic particles (reported here for the first time to the best of our knowledge). In addition, the proposed work might be favored over other synthesis techniques for bimetallic or solo nanomaterials due to challenging or

costly target fabrication, such as in the form of bimetallic bulk. However, the synthesized nanoparticles also comprise single target particles; therefore, the dual-pulsed laser-beam ablation system approach is not without its drawbacks. Possible causes for the generation of separate particles include the employment of two laser beams focused on a single target and the failure of the bubbles produced by each laser beam to collapse together during the beam adjustment procedure. In this study, Nd:YAG 1064 nm dual-pulsed laser ablation is studied for manufacturing plasmonic composites. The spectroscopic analysis, shape, size, compositions, and magnetic properties of dual-pulsed laser-assisted NPs were studied using UV-visible, TEM, XRD, and VSM, respectively. Finally, a near-infrared (808 nm) laser was used to examine the photothermal response of plasmonic-magnetic nanofluids and a control medium of pure water.

2. Experimental Setup

Figure 1 depicts the synthesis of NPs using a dual-pulsed laser ablation system. The Q-switched Nd:YAG 1064 nm laser with a pulse duration of 7 ns and a repetition rate of 10 Hz was used to obtain magneto-plasmonic particles. The dual-pulsed laser was achieved by using a polarizing beam splitter. A single-pulsed laser beam with an energy of 150 mJ is divided into two laser beams with a beam energy of 50 mJ and 100 mJ, respectively.

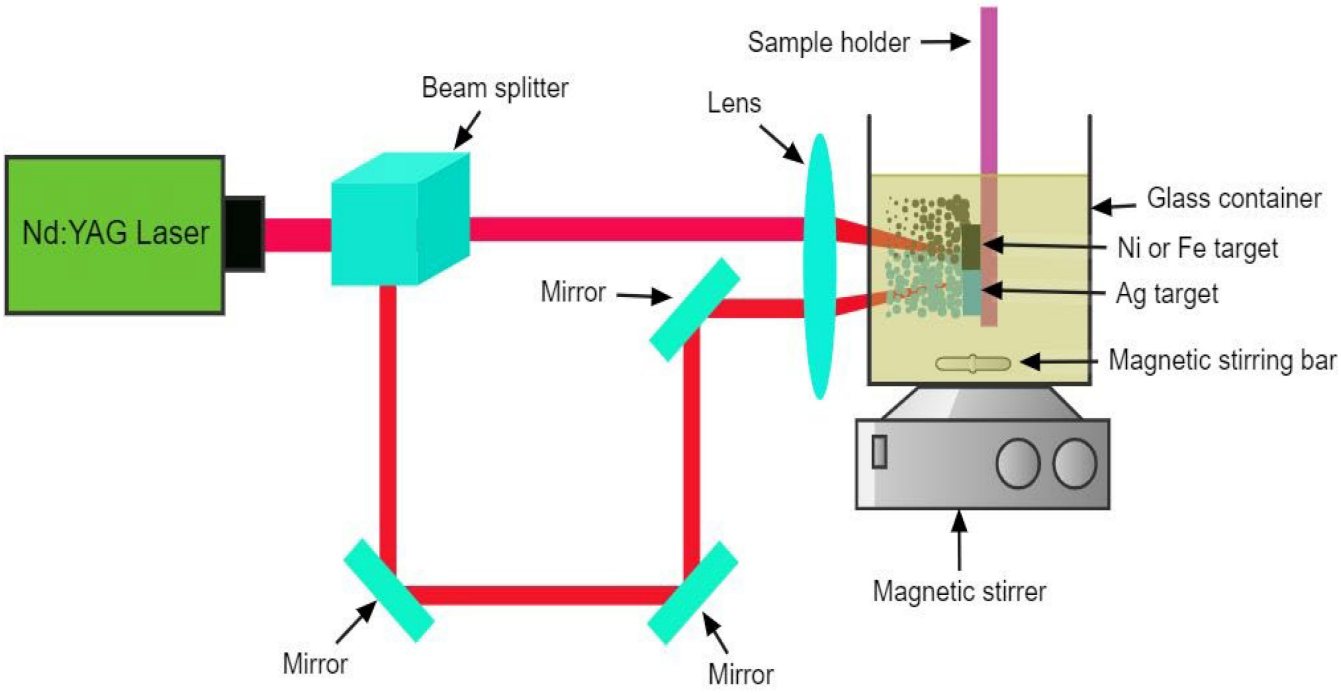

Figure 1. Dual-pulsed laser ablation system for the preparation of NPs.

Mirrors and a prism were used in order to achieve reflection of the laser beam. The lens was used to focus the beams with an identical diameter of 1.5 mm on a spot with a per-pulse energy of 50 mJ on Ag and 100 mJ on Ni or Fe double-bulk targets. These targets were attached side by side at the surface of a sample holder, which was dipped in a sample chamber filled with distilled water. The two separate targets, silver and nickel, having dimensions (3 mm × 3 mm) closely placed together, were used for dual-pulsed ablation of targets; the process was repeated for silver and iron targets (materials bought with a purity of 99.99% from ZhongNuo Advanced Materials Beijing, https://www.enfsolar.com/znxc-tech). The focused beams with a spot size of 1.5 mm were targeted at 50 mJ on Ag and 100 mJ on nickel in Ag and Ni targets. On Ag and Fe targets, 50 mJ on Ag and 100 mJ on iron were focused, respectively. The mechanism of particle formation is shown in Figure 2. Our previous work reported the identical anticipated mechanism for Ag and

Co targets [4]. Due to high temperature and pressure at the initial and collapse moments of the bubble, primary and agglomerated secondary particles are formed, and laser-generated bubbles can act as an ideal reactor for different kinds of particle formation [42]. The optical properties of synthesized NPs were examined within the 200–800 nm wavelength range using a UV/Vis-absorption spectrometer (T80-UV/VIS spectrometer, PG instrument Limited). Dried synthesized samples were used for testing magnetic properties using a vibrating sample magnetometer (VSM) (Lakeshore Model 7304). Transmission electron microscopy (TEM) (JEM-2100F) and X-ray diffraction (XRD) (Miniflex 600, Rigaku, Austin, TX, USA) were used to study the shape, size, and compositions of nanoparticles. The 808 nm laser (LWIRL-808-5 W) with operating powers of 1.240, 1.76, 2.36, 2.91, 3.5, and 4 W was used to study the photothermal response of distilled water and Ag/Ni and Ag/Fe nanofluids. The temperature elevation profiles were measured using a thermocouple (CENTER, 300 SERIES).

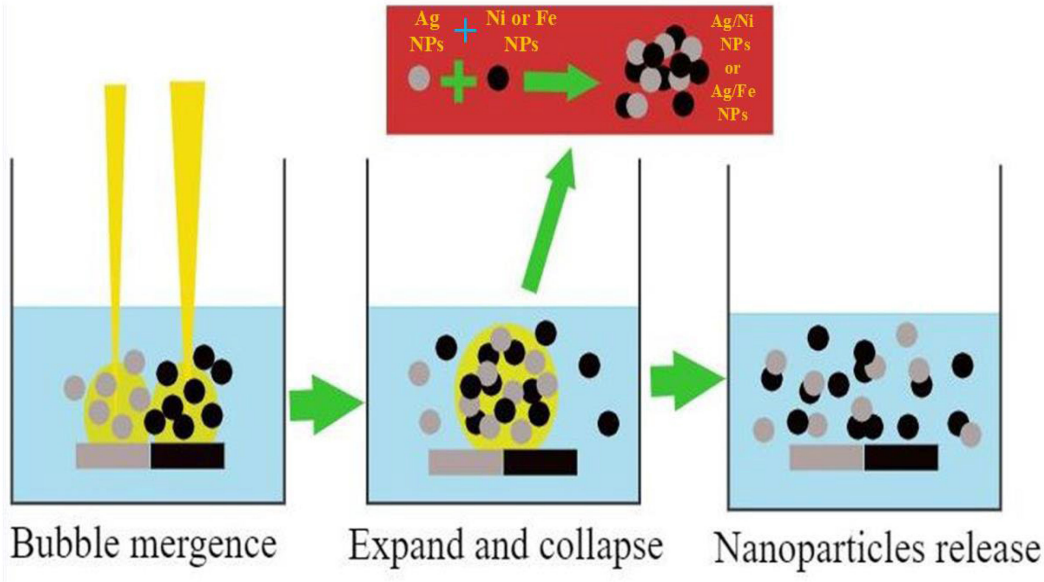

Figure 2. Preparation mechanism of anticipated NPs.

Synthesis Mechanism of NPs via Dual-Pulsed Laser

The supposed physical mechanism of nanoparticle synthesis using dual-pulsed laser ablation in liquid is plasma generation at high temperature and high pressure by the interaction of high-power laser beams with the surfaces of the targeted materials, which causes ionization, atomization, and decomposition of solvent molecules. The simultaneous application of two laser beams causes the formation of bubbles in the solution as a result of the transfer of energy from the plasma to the solution during the process of quickly quenching the plasma. During the process of plasma formation and quenching, emitted material specimens have the potential to engage in chemical interactions with reactive materials produced from targets and decomposed liquid molecules. Species formed undergo a transformation into particles as a result of a high collision rate caused by the high temperature and pressure. The cavitation bubbles burst when they reach their threshold volume as a result of a series of variations in expansion and contraction, and this resulted in the release of nanoparticles into the solution. These ligand-free reactive particles have the potential to generate a variety of different nanomaterials with distinct geometries. These active, ligand-free nanoparticles may form different types of nanoparticles with diverse geometries [43–46]. Fragmentation and possible core-shell or alloyed NPs formation result from the dual laser irradiation of the solution containing a wide variety of nanoparticles. To create alloy NPs, it is required for two separate NPs to come into direct physical contact with one another when the NPs are in the molten state [47].

3. Results and Discussion

3.1. Optical Properties of NPs Suspensions

Figure 3a,b show the results of a UV-visible spectroscopic examination performed to investigate the optical characteristics of Ag/Ni and Ag/Fe nanomaterials produced by dual laser beams. Firstly, the color transformation from a colorless distilled water solution after dual-laser beam ablation signaled the formation of NPs. In Figure 3a, we can see that the absorption peak of Ag/Ni NPs for LSPR occurs at 407 nm. The absorption peak we measured is consistent with the Ag/Ni absorption peaks reported in the literature [48,49], with some slight variations. The UV-visible spectrum of Ag/Fe NPs is shown in Figure 3b, and it is almost identical to the UV-Vis spectra presented in the literature [50]. The UV-Vis pattern of Ag/Fe NPs shows a broad absorption spectrum. Colloids generated by a laser ablation process at various energies also showed a wide absorption spectrum in their absorbance spectra [51].

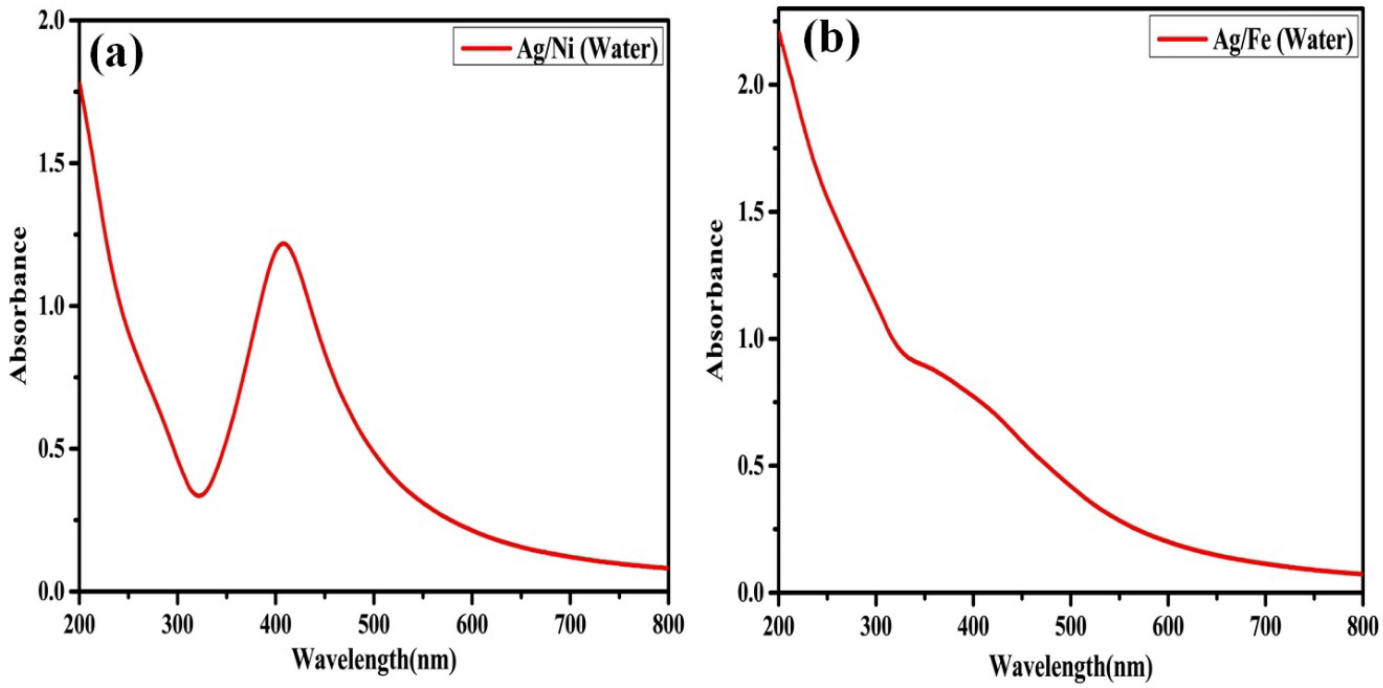

Figure 3. The absorption spectra of dual-pulsed laser-assisted nanoparticles are presented. (**a**) The UV-visible spectrum of Ag/Ni NPs. (**b**) The UV-visible spectrum of Ag/Fe NPs.

3.2. Magnetic Properties of NPs Synthesized via a Dual-Pulsed Laser System

The magnetic properties of dual-pulsed laser-generated Ag/Ni and Ag/Fe NPs were analyzed using the hysteresis loop of a VSM. As can be seen in Figure 4a, the saturation magnetization (M_s), remanent magnetization (M_r), and coercivity (H_c) of laser dual-beam assisted Ag/Ni NPs were measured to be 0.70 emu/g, 0.06 emu/g, and 94 Oe, respectively. The saturation magnetization, remanent magnetization, and coercivity values we obtained are consistent with those published by other researchers [52,53]. Figure 4b displays the saturation magnetization, remanent magnetization (M_r), and coercivity (H_c) values measured for Ag/Fe particles at 14.61 emu/g, 1.01 emu/g, and 65.35 Oe, respectively. In the case of Ag/Fe NPs, our measured values are consistent with those found in the literature [54–57]. Particles with such magnetic characteristics have a magnetic response and may be readily isolated or grouped with the help of an external magnetic field [58].

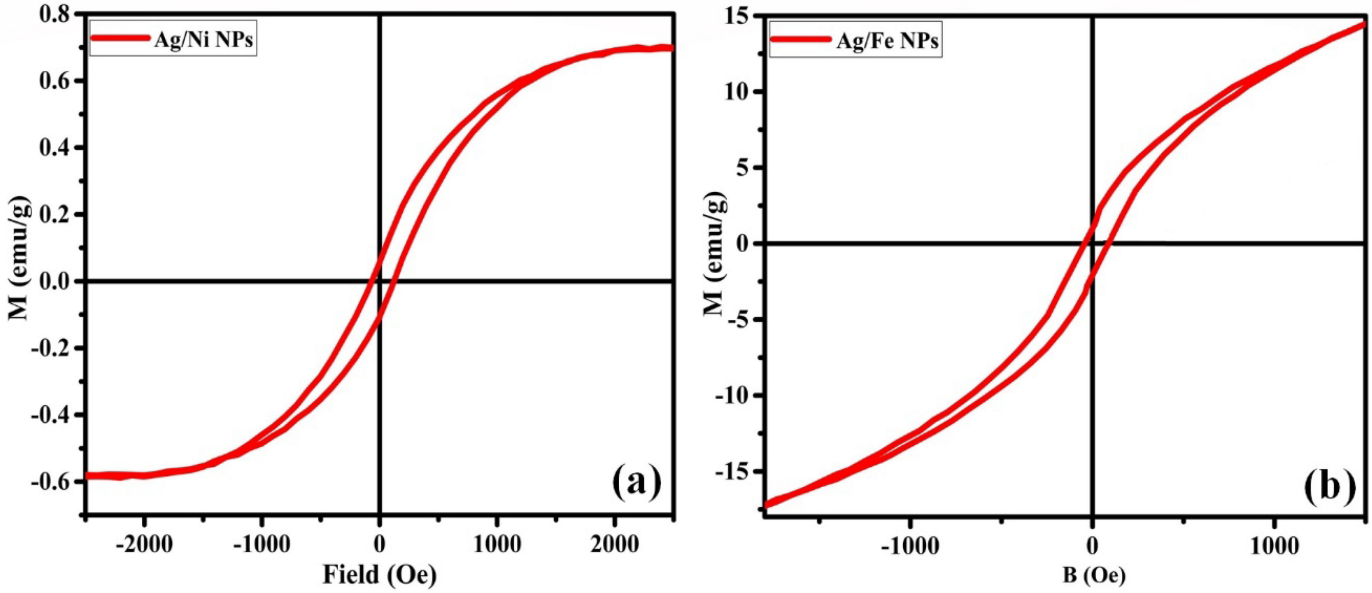

Figure 4. The magnetic hysteresis loops of dual-pulsed laser-assisted NPs are presented. (**a**) The magnetic properties of Ag/Ni NPs. (**b**) The magnetic properties of Ag/Fe NPs.

3.3. TEM of NPs Prepared by Dual-Pulsed Laser Ablation Setup

Micrographs and histograms of Ag/Ni NPs and Ag/Fe NPs, generated using a dual-pulsed laser arrangement, are shown in Figures 5 and 6, respectively. The TEM picture and the accompanying histogram of Ag/Ni nanoparticles are shown in Figure 5a,b. It can be seen in Figure 5a that the nanomaterials have a nearly spherical shape with a mean diameter of 7.3 nm. Diameters of 30 nm were reported for Ag/Ni composites synthesized using a microwave-assisted methodology [52], whereas in our instance, the size observed was less than that reported for Ag/Ni composites synthesized using a surfactant-assisted seedless method [49]. Ag/Fe particles were found to be spherical nanoparticles with a mean diameter of 11.5 nm, as seen in Figure 6a. Previous research [59] revealed spherical NPs with a diameter of 17 nm and longitudinal rod-shaped NPs with a width of 19 nm and a length of 23–127 nm. Recent work has revealed spherical Fe_3O_4/Ag nanoparticles with diameters between 15 and 30 nm [57], while prior work has seen spherical Fe_3O_4/Ag hybrid nanomaterials produced using the in situ reduction technique with a diameter of almost 10.41 nm [31].

3.4. XRD Analysis of NPs Generated by Dual-Pulsed Laser Ablation Apparatus

The XRD spectra of Ag/Ni and Ag/Fe particles generated with a dual-pulsed laser system are shown in Figure 7a,b, respectively. Based on the 82-0007 JCPDS card given to AgNiO2 nanocomposite, the diffraction peak 1 allocated at 35.5° correlates to crystalline planes (101). This is shown in Figure 7a, from left to right. Figure 7a shows that the diffraction peaks 2, 3, 5, and 6 correspond to the crystallographic planes (111), (200), (220), and (311), respectively, at 38.1°, 44.3°, 64.5°, and 77.4°, according to JCPDS card No. 04-0873 for Ag. Identical diffraction peaks were found, with slight changes, in the literature. [53,60–62]. Based on the data from JCPDS card 04-0850 [63], The diffraction peak for Ni NPs was measured to be 51.9°, which corresponds to the orientation of their crystalline planes (200). The XRD spectrum of Ag/Fe nanoparticles produced using a dual-pulsed laser apparatus is shown in Figure 7b. Crystalline planes (200) were identified by observing diffraction peaks (1, from left to right) at 44.6° in synthesized NPs; these values agree with the standard data according to PDF#99-0094, with some small discrepancies attributed to silver. The second diffraction peak was found at 72.5°, which corresponds to the reflection of Fe with crystalline planes (119), and the results agree with the reference data given in PDF#99-0060.

Figure 7a,b show the XRD data, which suggest that the particles generated in Ag and Ni and Ag and Fe targets were entirely composed of Ag and Ni and Ag and Fe with no other impurities present.

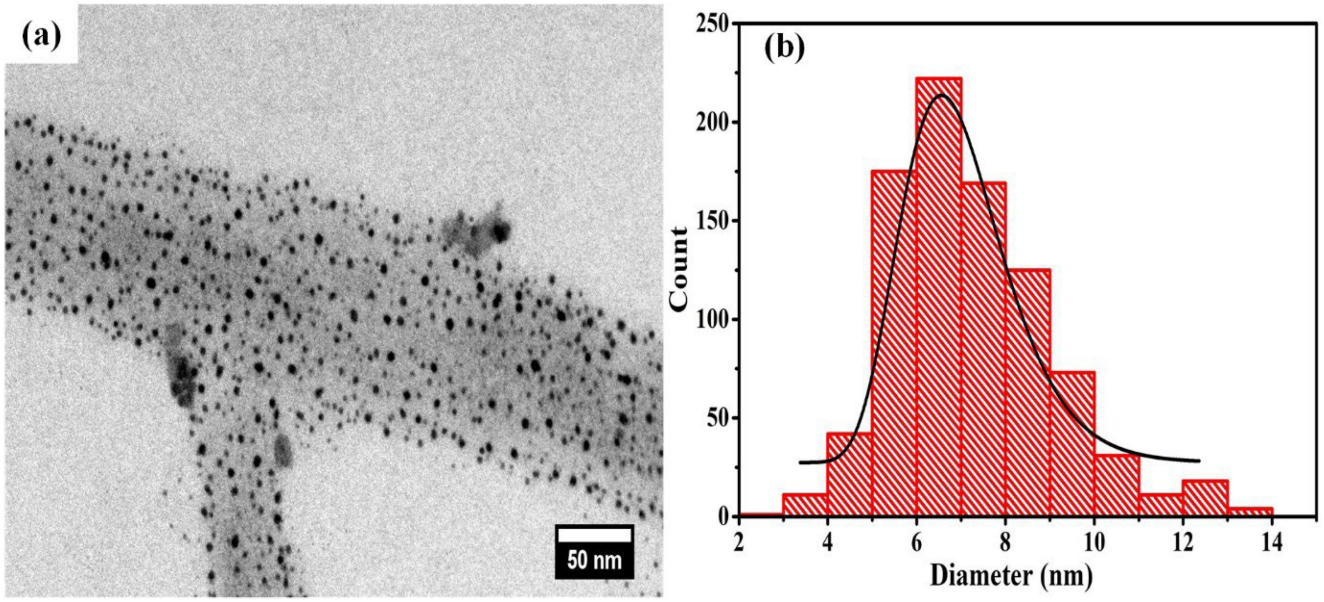

Figure 5. TEM image and corresponding histogram of Ag/Ni NPs synthesized using a dual-pulsed laser system are presented. (**a**) represents the TEM micrograph, and (**b**) indicate the corresponding histogram representing the particle size distribution.

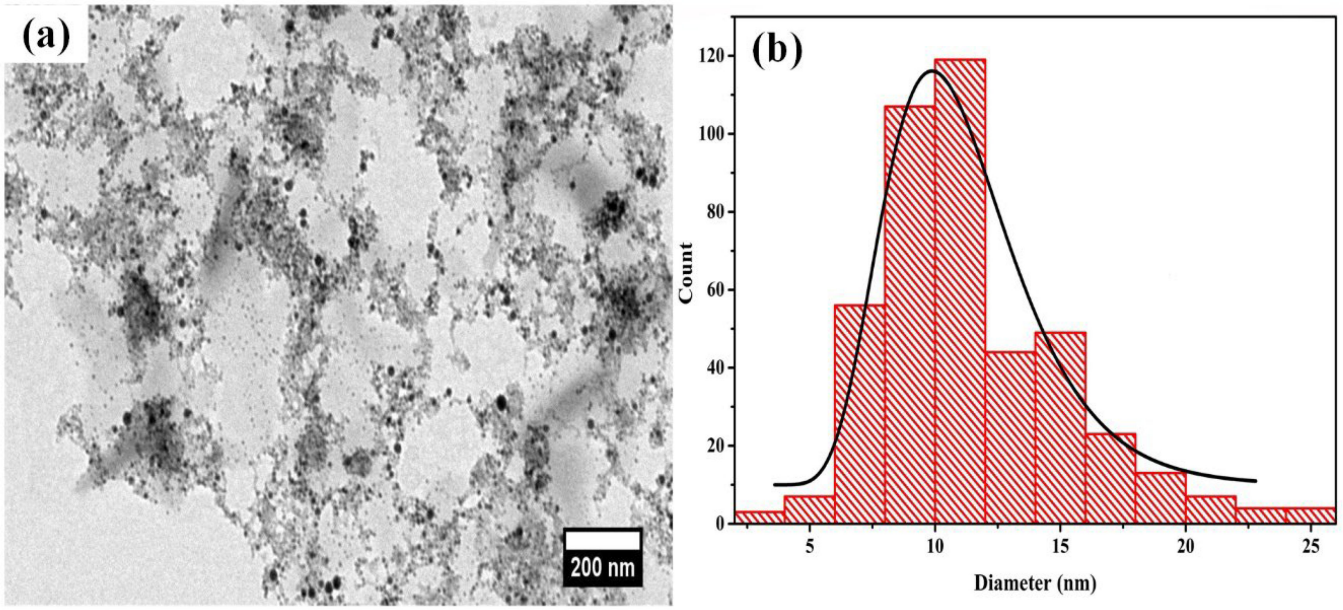

Figure 6. TEM image and histogram showing the size distribution of Ag/Fe NPs synthesized using a dual-pulsed laser setup are presented. (**a**) represents the TEM micrograph, and (**b**) is the histogram showing the particle size distribution analysis for the corresponding.

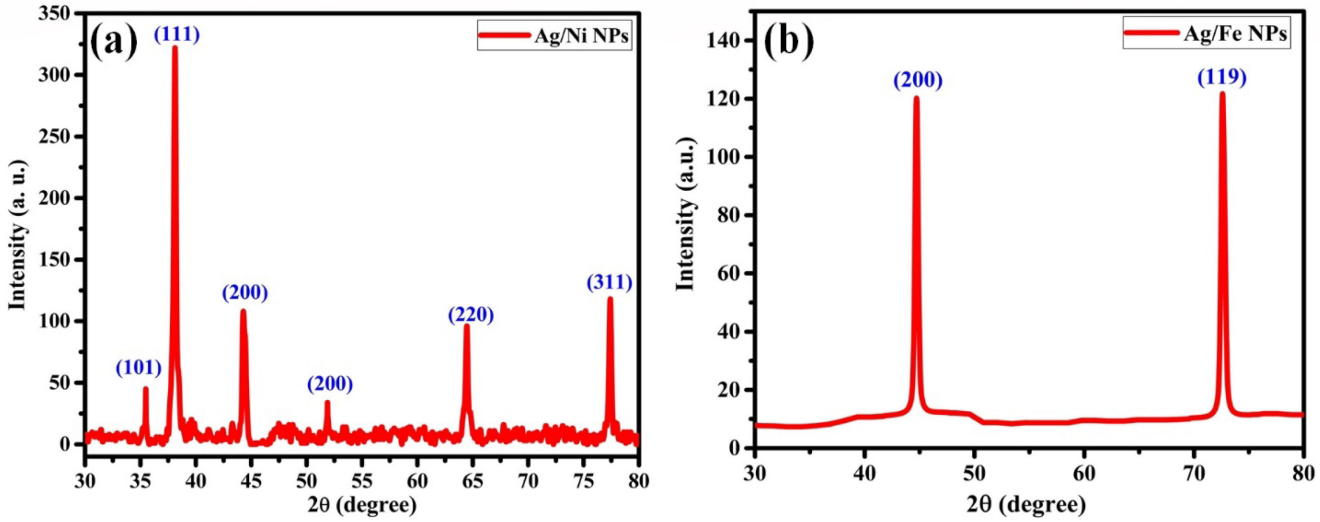

Figure 7. XRD spectra of particles produced by dual-pulsed laser ablation are presented. (**a**) The XRD spectrum of Ag/Ni particles. (**b**) The XRD spectrum of Ag/Fe particles.

3.5. Photothermal Performance of Ag/Ni and Ag/Fe Nanofluids

According to the findings presented in the review [64], controlling the interactions between nanoparticles and light greatly depends on the shape of the nanoparticles used in hyperthermia. Increasing the efficiency of the light-heat conversion may also be accomplished by adjusting the nanoparticles' size, and it has been shown that different sized nanoparticles absorb light of different wavelengths [65]. The photothermal conversion efficiency of iron oxide nanoparticles, where the thermal response is predominantly owing to electronic transitions between d-orbitals of nearby Fe ions inside the lattice, deviates from the normal photo-induced hyperthermia [66]. In order to deactivate the SARS-CoV-2 virus, surface temperatures on the textiles were raised to as high as 150 °C by photothermal activation of spherical silver nanoparticles that ranged in diameter from 5 to 10 nm [5]. For the purpose of focused photothermal cancer treatment, plasmonic Ag nanoparticles with rounded forms and a diameter of 35.4 ± 1.6 nm have been reported [67]. The photothermal response study of spherical Ag/Ni and Ag/Fe nanoparticles, each having a mean diameter of 7.3 nm and 11.5 nm, respectively, has been investigated in the presented work.

Evaluations of photothermal conversion have been performed on Ag/Ni and Ag/Fe nanofluids, in addition to water as a reference medium, as a function of laser power and laser irradiation duration. The brief photothermal conversion property process is described. A test tube containing 1.5 mL of NPs suspension was sonicated for one minute to make it homogeneous. The sonicated nanofluids were exposed to an NIR (808 nm) laser. When the laser beam is coupled with nanoparticles, it is divided into two major parts. Non-radiative decay refers to the process through which NPs consume the light that they absorb. Radiative decay refers to the re-emitted portion of the light that has either a different frequency than the absorbed photon (Raman scattering) or the same frequency (Raleigh scattering). The nanoparticles generate heat because they absorb some of the light that hits them. The absorption of photons from irradiating light gives the electrons a lot of energy, creating an unstable environment inside the nanoparticles. This imbalance causes energy transfer through electron-phonon relaxation. As the phonons' energy is dissipated by phonon-phonon scattering into the surrounding media, the temperature of that medium rises even more [13,68–71]. The assessment of nano-suspension for photothermal conversion is described in detail in the review by the authors in [72]. To test the hypothesis that the amount of heat produced is proportional to the power of the laser, we examined the photothermal conversion properties of nanofluids using a continuous NIR 808 nm laser (see Figure 8 for further details on the experimental setup).

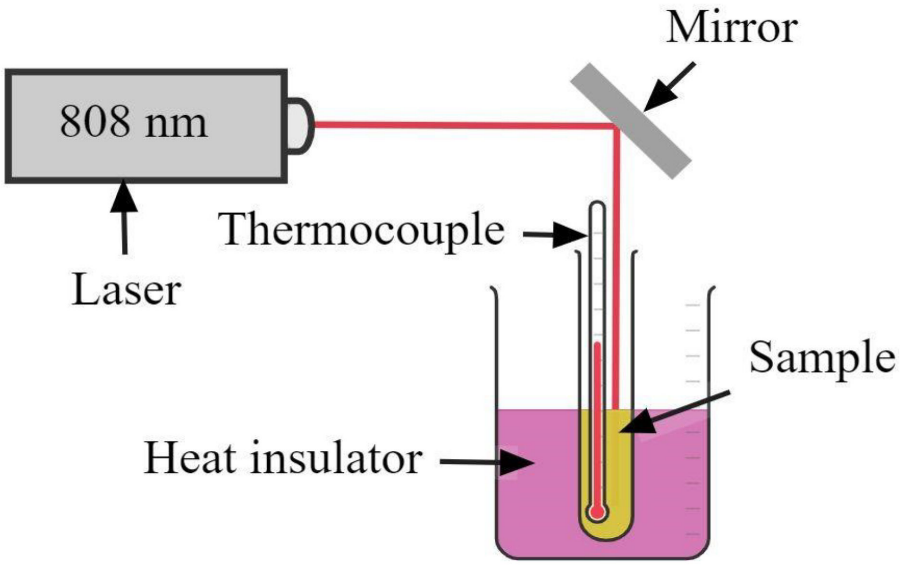

Figure 8. Setup for photothermal conversion response evaluation of nanofluids and pure water.

The analytical heating model for the photothermal conversion performance of nanofluid was calculated as the following equation [73,74]:

$$\eta = \frac{hS\,(T_{max} - T_{surr}) - Q_o}{I(1 - 10^{-A_{808}})} \quad (1)$$

The terms I, h, T_{max}, T_{surr}, and S, represent the power of the incident laser, the heat-transfer coefficient, the maximum temperature, the ambient room temperature, and the container surface area. Q_o is the baseline energy, and it has a recorded value of 5.4 mW with pure water and a quartz cuvette without NPs. A_{808} and η denote the absorbance of NPs at 808 nm and the photothermal conversion efficiency of NP, respectively. It was concluded that the heat production is directly proportional to laser power and the number of particles [75].

$$SAR = NQ_{nano} = NC_{abs}\,I \quad (2)$$

where Q_{nano} is the amount of heat produced by a single particle, N is the number of nanoparticles in a cubic meter, C_{abs} is the individual nanoparticle cross-section area, and I is the laser power density. Equation (2) illustrates that heat generation is a function of laser power density. NIR lasers have the advantage of deep penetration of light into a biological medium, and the NIR region is also known as the biological window [76]. Different methodologies have been adopted in shifting from the UV absorption region to the NIR regions, such as for adjusting nanoparticle compositions [70], shapes [77], and sizes [78]. Iron oxide exhibits a characteristic peak at 205 nm [79], and Fe_3O_4 NPs clusters were used for a photothermal response study using the NIR 808 nm laser [80]. Figure 9a,b show the temperature increase outline for Ag/Ni and Ag/Fe nanofluids at various times and power levels of the NIR 808 laser. Figure 9c represents the water temperature distribution and was taken as a reference [4]. Temperature measurements of Ag/Ni and Ag/Fe nanofluids showed that they were, respectively, 26 °C and 24 °C before being exposed to laser light. Figure 9 displays the temperatures reached by the Ag/Ni nanofluid at 31.5, 35.5, 39.3, 40.4, and 42.6 °C after 3, 6, 9, 12, and 15 min of exposure to a 1.24 W laser. The corresponding temperatures for Ag/Fe nanofluid were 35.1, 40, 42.6, 44.9, and 45.2 °C, as shown in Figure 9b. Using a laser power of 1.24 W, we found that the saturation temperatures for Ag/Ni and Ag/Fe nanofluids were 48.9 °C and 52 °C, respectively.

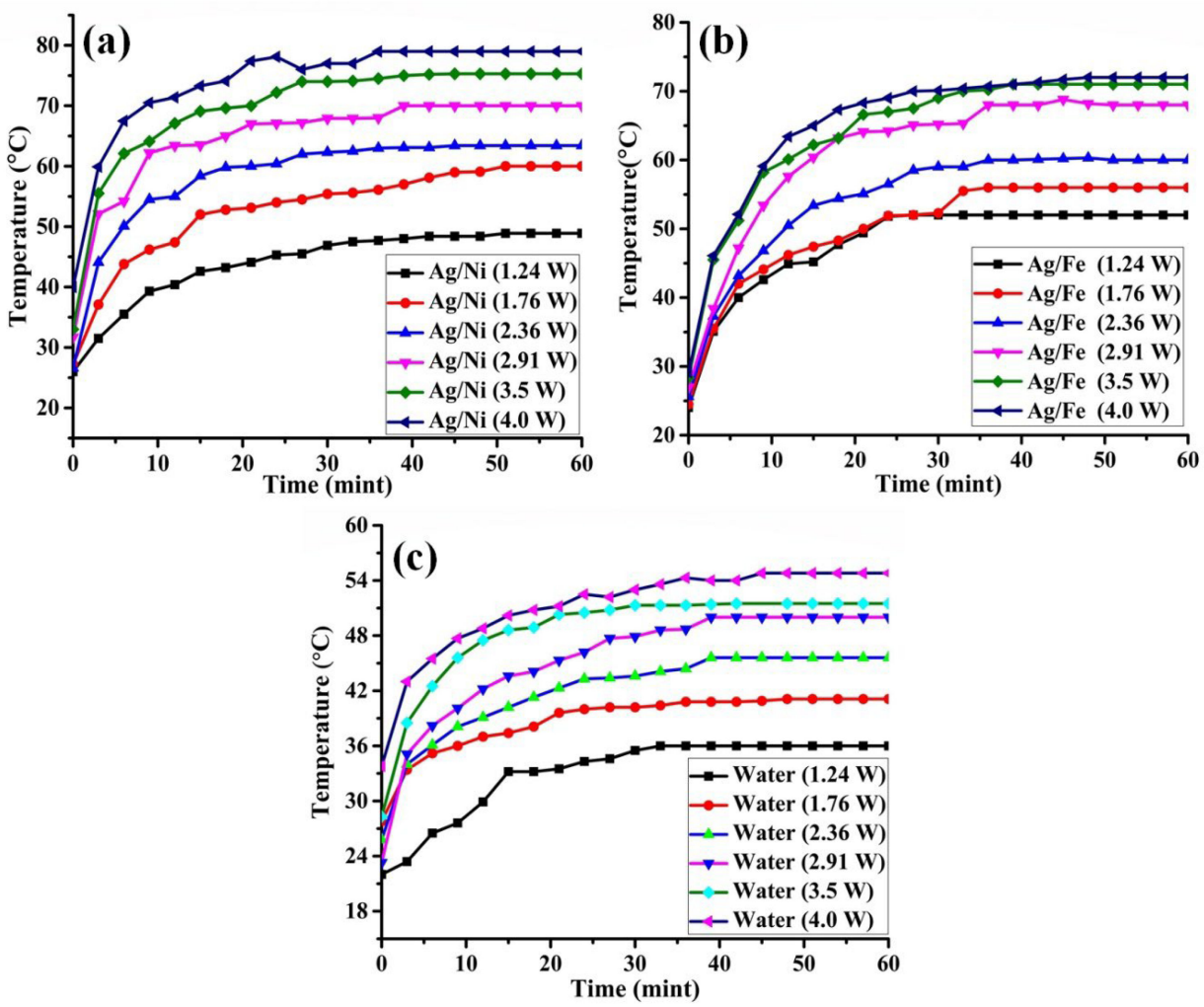

Figure 9. The temperature rises as a function of the power and time of an irradiated NIR 808 nm laser. (**a**) The temperature rise profiles for Ag/Ni nanofluid. (**b**) The temperature rises trend for Ag/Fe nanofluid. (**c**) The temperature rise outlines for the distilled water.

The saturated temperatures of Ag/Ni suspension were measured as 60, 63.4, 70, 75.3, and 79 °C at laser powers of 1.76, 2.36, 2.91, 3.5, and 4 W, respectively. Similarly, the peak temperatures for Ag/Fe nanofluid were recorded as 56, 60, 68, 71, and 72 °C at laser powers of 1.76, 2.36, 2.91, 3.5, and 4 W, respectively. To put it another way, the efficiency of Ag/Ni nanofluid is greater than that of Ag/Fe nanofluid. The marked difference in high-temperature profiles of NPs suspensions and water alone can be revealed in the corresponding graph profiles. The possible cause for these trends and changes is the plasmonic hyperthermia response of nanomaterials. The trends in temperatures showed that the temperature of the NPs suspensions increased far more quickly than the temperature of the water alone. For Ag/Ag_2S NPs, a similar pattern was described [70]. Similar to the previous reports on MoS_2-PVP suspension [81] and gold nanoshells fluid [82], we found that the temperature rose rapidly with increasing laser power in the present study. With continued irradiation, the temperature of the nanofluid first increased sharply before stabilizing at a lower value. A similar trend was also observed in previous literature [83]. The fast temperature increases of Ag-rGO and graphene oxide begin to settle down after a certain time due to the dissipation of heat and absorption of energy from the incoming laser beam [84].

4. Conclusions

Ag/Ni and Ag/Fe nanomaterials have been synthesized using the environmentally friendly and non-polluting dual-pulsed Q-switched Nd:YAG laser ablation technique. Synthesized nanomaterials have been shown to display optical and magnetic characteristics, proving their dual nature. TEM analysis revealed that both Ag/Ni and Ag/Fe nanoparticles have a spherical shape with a mean diameter of 7.3 nm and 11.5 nm, respectively. XRD examination confirmed that the Ag and Ni and Ag and Fe targets successfully synthesized pure Ag/Ni and Ag/Fe particles. Peak temperatures of 48.9, 60, 63.4, 70, 75, and 79 °C for Ag/Ni nanofluid and 52, 56, 60, 68, 71, and 72 °C for Ag/Fe nanofluid were attained when the generated nanoparticles were subjected to an NIR 808 nm laser with operating powers of 1.24, 1.76, 2.36, 2.91, 3.5, and 4 W, respectively. The temperature profiles of water and nanofluids at varying laser powers all showed an encouraging upward trend. However, it was shown that NPs suspensions cause a greater rise in temperature than water alone. The rapid rise in temperature observed for Ag/Ni and Ag/Fe nanoparticles at higher corresponding laser powers demonstrates that they are more responsive to photothermal conversion than water. Applications benefiting from the photothermal conversion response of multifunctional materials include targeted and controlled cancer hyperthermia. However, they could also be used in other fields, such as liquid crystals, as a dopant in order to tune their optical (linear/non-linear), electro-optical, and dielectric properties.

Author Contributions: Conceptualization, I.A., J.C., Y.P. and Z.S.; methodology, A.A.S. and A.K.S.; validation, S.A.K., Y.J., S.J.G. and Y.F.; investigation, A.K.S. and S.J.G.; resources, Y.J. and A.A.S.; data curation, Y.J., A.A.S., A.K.S., S.J.G., M.N.B.J., Y.P. and Z.S.; writing—original draft preparation, I.A. and Z.S.; writing—review and editing, I.A., S.A.K., M.N.B.J., Y.F. and Y.P.; supervision, J.C. and Z.S.; project administration, J.C. and Y.P.; funding acquisition, S.J.G. and M.N.B.J. All authors have read and agreed to the published version of the manuscript.

Funding: This work was funded from Princess Nourah bint Abdulrahman University Researchers Supporting Project number (PNURSP2023R108), Princess Nourah Bint Abdulrahman University, Riyadh, Saudi Arabia.

Institutional Review Board Statement: Not applicable.

Informed Consent Statement: Not applicable.

Data Availability Statement: The data that support the findings of this study are available from the corresponding author upon reasonable request.

Conflicts of Interest: The authors declare that there is no conflict of interest regarding the publication of this article.

References

1. Ali Bhatti, M.; Shah, A.A.; Almani, K.F.; Tahira, A.; Chalangar, S.E.; dad Chandio, A.; Nur, O.; Willander, M.; Ibupoto, Z.H. Efficient photo catalysts based on silver doped ZnO nanorods for the photo degradation of methyl orange. *Ceram. Int.* **2019**, *45*, 23289–23297. [CrossRef]
2. Yeshchenko, O.A.; Golovynskyi, S.; Kudrya, V.Y.; Tomchuk, A.V.; Dmitruk, I.M.; Berezovska, N.I.; Teselko, P.O.; Zhou, T.; Xue, B.; Golovynska, I.; et al. Laser-Induced Periodic Ag Surface Structure with Au Nanorods Plasmonic Nanocavity Metasurface for Strong Enhancement of Adenosine Nucleotide Label-Free Photoluminescence Imaging. *ACS Omega* **2020**, *5*, 14030–14039. [CrossRef]
3. Khurana, K.; Jaggi, N. Localized Surface Plasmonic Properties of Au and Ag Nanoparticles for Sensors: A Review. *Plasmonics* **2021**, *16*, 981–999. [CrossRef]
4. Ali, I.; Pan, Y.; Lin, Y.; Jamil, Y.; Hu, J.; Gan, Z.; Chen, J.; Shen, Z. Synthesis of Ag/Co Nanoparticles by Dual Pulsed Laser Ablation for Synergistic Photothermal Study. *Appl. Phys. A* **2021**, *127*, 632. [CrossRef]
5. MacPhee, J.; Kinyenye, T.; MacLean, B.J.; Bertin, E.; Hallett-Tapley, G.L. Investigating the Photothermal Disinfecting Properties of Light-Activated Silver Nanoparticles. *Ind. Eng. Chem. Res.* **2021**, *60*, 17390–17398. [CrossRef]
6. Choudhary, A.; Singh, G.; Biradar, A.M. Advances in Gold Nanoparticle-Liquid Crystal Composites. *Nanoscale* **2014**, *6*, 7743–7756. [CrossRef] [PubMed]
7. Boles, M.A.; Ling, D.; Hyeon, T.; Talapin, D.V. Erratum: The Surface Science of Nanocrystals. *Nat. Mater.* **2016**, *15*, 364. [CrossRef] [PubMed]

8. Coursault, D.; Sule, N.; Parker, J.; Bao, Y.; Scherer, N.F. Dynamics of the Optically Directed Assembly and Disassembly of Gold Nanoplatelet Arrays. *Nano Lett.* **2018**, *18*, 3391–3399. [CrossRef]
9. Zhu, W.; Esteban, R.; Borisov, A.G.; Baumberg, J.J.; Nordlander, P.; Lezec, H.J.; Aizpurua, J.; Crozier, K.B. Quantum Mechanical Effects in Plasmonic Structures with Subnanometre Gaps. *Nat. Commun.* **2016**, *7*, 11495. [CrossRef]
10. Pinheiro, T.; Marques, A.C.; Carvalho, P.; Martins, R.; Fortunato, E. Paper Microfluidics and Tailored Gold Nanoparticles for Nonenzymatic, Colorimetric Multiplex Biomarker Detection. *ACS Appl. Mater. Interfaces* **2021**, *13*, 3576–3590. [CrossRef]
11. Zhang, Y.; Chen, B.; Xu, S.; Li, X.; Zhang, J.; Sun, J.; Zheng, H.; Tong, L.; Sui, G.; Zhong, H.; et al. Dually Functioned Core-Shell $NaYF_4$:Er^{3+}/Yb^{3+}@$NaYF_4$:Tm^{3+}/Yb^{3+} Nanoparticles as Nano-Calorifiers and Nano-Thermometers for Advanced Photothermal Therapy. *Sci. Rep.* **2017**, *7*, 11849. [CrossRef] [PubMed]
12. Zheng, X.; Xing, D.; Zhou, F.; Wu, B.; Chen, W.R. Indocyanine Green-Containing Nanostructure as near Infrared Dual-Functional Targeting Probes for Optical Imaging and Photothermal Therapy. *Mol. Pharm.* **2011**, *8*, 447–456. [CrossRef] [PubMed]
13. Cherukula, K.; Lekshmi, K.M.; Uthaman, S.; Cho, K.; Cho, C.S.; Park, I.K. Multifunctional Inorganic Nanoparticles: Recent Progress in Thermal Therapy and Imaging. *Nanomaterials* **2016**, *6*, 76. [CrossRef]
14. Resch-Genger, U.; Grabolle, M.; Cavaliere-Jaricot, S.; Nitschke, R.; Nann, T. Quantum Dots versus Organic Dyes as Fluorescent Labels. *Nat. Methods* **2008**, *5*, 763–775. [CrossRef]
15. Brezovich, I.A.; Young, J.H. Hyperthermia with Implanted Electrodes. *Med. Phys.* **1981**, *8*, 79–84. [CrossRef]
16. Robins, H.I.; Rushing, D.; Kutz, M.; Tutsch, K.D.; Tiggelaar, C.L.; Paul, D.; Spriggs, D.; Kraemer, C.; Gillis, W.; Feierabend, C.; et al. Phase I Clinical Trial of Melphalan and 41.8 °C Whole-Body Hyperthermia in Cancer Patients. *J. Clin. Oncol.* **1997**, *15*, 158–164. [CrossRef] [PubMed]
17. Douple, E.B.; Strohbehn, J.W.; Bowers, E.D.; Walsh, J.E. Cancer Therapy with Localized Hyperthermia Using an Invasive Microwave System. *J. Microw. Power* **1979**, *14*, 181–186. [CrossRef] [PubMed]
18. Bhana, S.; Lin, G.; Wang, L.; Starring, H.; Mishra, S.R.; Liu, G.; Huang, X. Near-Infrared-Absorbing Gold Nanopopcorns with Iron Oxide Cluster Core for Magnetically Amplified Photothermal and Photodynamic Cancer Therapy. *ACS Appl. Mater. Interfaces* **2015**, *7*, 11637–11647. [CrossRef]
19. Ovejero, J.G.; Morales, I.; De La Presa, P.; Mille, N.; Carrey, J.; Garcia, M.A.; Hernando, A.; Herrasti, P. Hybrid Nanoparticles for Magnetic and Plasmonic Hyperthermia. *Phys. Chem. Chem. Phys.* **2018**, *20*, 24065–24073. [CrossRef]
20. Jaque, D.; Vetrone, F. Luminescence Nanothermometry. *Nanoscale* **2012**, *4*, 4301–4326. [CrossRef]
21. Quek, C.H.; Leong, K.W. Near-Infrared Fluorescent Nanoprobes for in Vivo Optical Imaging. *Nanomaterials* **2012**, *2*, 92–112. [CrossRef]
22. Zhou, Z.; Sun, Y.; Shen, J.; Wei, J.; Yu, C.; Kong, B.; Liu, W.; Yang, H.; Yang, S.; Wang, W. Iron/Iron Oxide Core/Shell Nanoparticles for Magnetic Targeting MRI and near-Infrared Photothermal Therapy. *Biomaterials* **2014**, *35*, 7470–7478. [CrossRef] [PubMed]
23. Shen, S.; Wang, S.; Zheng, R.; Zhu, X.; Jiang, X.; Fu, D.; Yang, W. Magnetic Nanoparticle Clusters for Photothermal Therapy with Near-Infrared Irradiation. *Biomaterials* **2015**, *39*, 67–74. [CrossRef] [PubMed]
24. Chu, M.; Shao, Y.; Peng, J.; Dai, X.; Li, H.; Wu, Q.; Shi, D. Near-Infrared Laser Light Mediated Cancer Therapy by Photothermal Effect of Fe_3O_4 Magnetic Nanoparticles. *Biomaterials* **2013**, *34*, 4078–4088. [CrossRef]
25. Pązik, R.; Zachanowicz, E.; Pożniak, B.; Małecka, M.; Zięcina, A.; Marciniak, Ł. Non-Contact Mn1-XNixFe_2O_4 Ferrite Nano-Heaters for Biological Applications-Heat Energy Generated by NIR Irradiation. *RSC Adv.* **2017**, *7*, 18162–18171. [CrossRef]
26. Manikandan, R.; Manikandan, B.; Raman, T.; Arunagirinathan, K.; Prabhu, N.M.; Jothi Basu, M.; Perumal, M.; Palanisamy, S.; Munusamy, A. Biosynthesis of Silver Nanoparticles Using Ethanolic Petals Extract of Rosa Indica and Characterization of Its Antibacterial, Anticancer and Anti-Inflammatory Activities. *Spectrochim. Acta-Part A Mol. Biomol. Spectrosc.* **2015**, *138*, 120–129. [CrossRef]
27. Suganya, K.S.U.; Govindaraju, K.; Kumar, V.G.; Dhas, T.S.; Karthick, V.; Singaravelu, G.; Elanchezhiyan, M. Size Controlled Biogenic Silver Nanoparticles as Antibacterial Agent against Isolates from HIV Infected Patients. *Spectrochim. Acta Part A Mol. Biomol. Spectrosc.* **2015**, *144*, 266–272. [CrossRef] [PubMed]
28. Zhang, X.F.; Liu, Z.G.; Shen, W.; Gurunathan, S. Silver Nanoparticles: Synthesis, Characterization, Properties, Applications, and Therapeutic Approaches. *Int. J. Mol. Sci.* **2016**, *17*, 1534. [CrossRef]
29. Lee, C.C.; Chen, D.H. Large-Scale Synthesis of Ni-Ag Core-Shell Nanoparticles with Magnetic, Optical and Anti-Oxidation Properties. *Nanotechnology* **2006**, *17*, 3094–3099. [CrossRef]
30. Guo, H.; Chen, Y.; Chen, X.; Wen, R.; Yue, G.-H.; Peng, D.-L. Facile Synthesis of Near-Monodisperse Ag@ Ni Core–Shell Nanoparticles and Their Application for Catalytic Generation of Hydrogen. *Nanotechnology* **2011**, *22*, 195604. [CrossRef]
31. Ding, Q.; Liu, D.; Guo, D.; Yang, F.; Pang, X.; Che, R.; Zhou, N.; Xie, J.; Sun, J.; Huang, Z. Shape-Controlled Fabrication of Magnetite Silver Hybrid Nanoparticles with High Performance Magnetic Hyperthermia. *Biomaterials* **2017**, *124*, 35–46. [CrossRef]
32. Santhi, K.; Kumarsan, D.; Vengidusamy, N.; Arumainathan, S. Electrochemical Alloying of Immiscible Ag and Co for Their Structural and Magnetic Analyses. *J. Magn. Magn. Mater.* **2017**, *433*, 202–208. [CrossRef]
33. Tancredi, P.; Moscoso Londoño, O.; Rivas Rojas, P.C.; Wolff, U.; Socolovsky, L.M.; Knobel, M.; Muraca, D. Strategies to Tailor the Architecture of Dual Ag/Fe-Oxide Nano-Heterocrystals-Interfacial and Morphology Effects on the Magnetic Behavior. *J. Phys. D Appl. Phys.* **2018**, *51*, 295303. [CrossRef]

34. Jing, J.J.; Xie, J.; Chen, G.Y.; Li, W.H.; Zhang, M.M. Preparation of Nickel–Silver Core–Shell Nanoparticles by Liquid-Phase Reduction for Use in Conductive Paste. *J. Exp. Nanosci.* **2015**, *10*, 1347–1356. [CrossRef]
35. Auten, B.J.; Hahn, B.P.; Vijayaraghavan, G.; Stevenson, K.J.; Chandler, B.D. Preparation and Characterization of 3 nm Magnetic NiAu Nanoparticles. *J. Phys. Chem. C* **2008**, *112*, 5365–5372. [CrossRef]
36. Barmina, E.V.; Shafeev, G.A. Formation of Core–Shell Fe@Al Nanoparticles by Laser Irradiation of a Mixture of Colloids in Ethanol. *Quantum Electron.* **2018**, *48*, 637–640. [CrossRef]
37. Boyer, P.; Ménard, D.; Meunier, M. Nanoclustered Co−Au Particles Fabricated by Femtosecond Laser Fragmentation in Liquids. *J. Phys. Chem. C* **2010**, *114*, 13497–13500. [CrossRef]
38. Messina, G.C.; Sinatra, M.G.; Bonanni, V.; Brescia, R.; Alabastri, A.; Pineider, F.; Campo, G.; Sangregorio, C.; Li-Destri, G.; Sfuncia, G.; et al. Tuning the Composition of Alloy Nanoparticles Through Laser Mixing: The Role of Surface Plasmon Resonance. *J. Phys. Chem. C* **2016**, *120*, 12810–12818. [CrossRef]
39. Wagener, P.; Jakobi, J.; Rehbock, C.; Chakravadhanula, V.S.K.; Thede, C.; Wiedwald, U.; Bartsch, M.; Kienle, L.; Barcikowski, S. Solvent-Surface Interactions Control the Phase Structure in Laser-Generated Iron-Gold Core-Shell Nanoparticles. *Sci. Rep.* **2016**, *6*, 23352. [CrossRef]
40. Amendola, V.; Scaramuzza, S.; Agnoli, S.; Granozzi, G.; Meneghetti, M.; Campo, G.; Bonanni, V.; Pineider, F.; Sangregorio, C.; Ghigna, P.; et al. Laser Generation of Iron-Doped Silver Nanotruffles with Magnetic and Plasmonic Properties. *Nano Res.* **2015**, *8*, 4007–4023. [CrossRef]
41. Muniz-Miranda, M.; Gellini, C.; Giorgetti, E.; Margheri, G. Bifunctional Fe_3O_4/Ag Nanoparticles Obtained by Two-Step Laser Ablation in Pure Water. *J. Colloid Interface Sci.* **2017**, *489*, 100–105. [CrossRef] [PubMed]
42. Liu, K.; Chen, J.; Qu, H.; Dong, Y.; Gao, Y.; Liu, J.; Liu, X.; Zou, Y.; Zeng, H. Bubble Dimer Dynamics Induced by Dual Laser Beam Ablation in Liquid. *Appl. Phys. Lett.* **2018**, *113*, 021902. [CrossRef]
43. Zhang, D.; Liu, J.; Liang, C. Perspective on How Laser-Ablated Particles Grow in Liquids. *Sci. China Phys. Mech. Astron.* **2017**, *60*, 074201. [CrossRef]
44. Shukri, W.N.W.; Bidin, N.; Islam, S.; Krishnan, G. Synthesis of Au–Ag Alloy Nanoparticles in Deionized Water by Pulsed Laser Ablation Technique. *J. Nanosci. Nanotechnol.* **2018**, *18*, 4841–4851. [CrossRef]
45. Santagata, A.; National, I.; Guarnaccio, A.; National, I.; Valyon, J. Production of Silver-Silica Core-Shell Nanocomposites Using Ultra-Short Pulsed Laser Ablation in Nanoporous Aqueous Silica Colloidal Solutions. *J. Phys. D Appl. Phys.* **2015**, *48*, 205304. [CrossRef]
46. Sakthisabarimoorthi, A.; Dhas, S.M.B.; Jose, M. Nonlinear optical properties of Ag@ SiO2 core-shell nanoparticles investigated by continuous wave He-Ne laser. *Mater. Chem. Phys.* **2018**, *212*, 224–229. [CrossRef]
47. Serkov, A.A.; Kuzmin, P.G.; Shafeev, G.A. Laser-Induced Agglomeration of Gold and Silver Nanoparticles Dispersed in Liquid. *Chem. Phys. Lett.* **2016**, *647*, 68–72. [CrossRef]
48. Zhou, H.; Li, Y.; Huang, J.; Fang, C.; Dan, S.; Kuang, Y. Ag-Ni Alloy Nanoparticles for Electrocatalytic Reduction of Benzyl Chloride. *Trans. Nonferrous Met. Soc. China* **2015**, *25*, 4001–4007. [CrossRef]
49. Alruqi, S.S.; Al-Thabaiti, S.A.; Malik, M.A.; Khan, Z. Role of Surfactants: One Step Facile Synthesis of Hetero Structured Ag-Ni Alloy by Seed Less Approach. *Coll. Surf. A Physicochem. Eng. Asp.* **2018**, *540*, 36–47. [CrossRef]
50. Chiou, J.R.; Lai, B.H.; Hsu, K.C.; Chen, D.H. One-Pot Green Synthesis of Silver/Iron Oxide Composite Nanoparticles for 4-Nitrophenol Reduction. *J. Hazard. Mater.* **2013**, *248–249*, 394–400. [CrossRef] [PubMed]
51. Rivera-Chaverra, M.J.; Restrepo-Parra, E.; Acosta-Medina, C.D.; Mello, A.; Ospina, R. Synthesis of Oxide Iron Nanoparticles Using Laser Ablation for Possible Hyperthermia Applications. *Nanomaterials* **2020**, *10*, 2099. [CrossRef]
52. Ger, T.-R.; Huang, H.-T.; Huang, C.-Y.; Liu, W.-C.; Lai, J.-Y.; Liu, B.-T.; Chen, J.-Y.; Hong, C.-W.; Chen, P.-J.; Lai, M.-F. Comparing the Magnetic Property of Shell Thickness Controlled of Ag-Ni Core-Shell Nanoparticles. *J. Appl. Phys.* **2014**, *115*, 17B528. [CrossRef]
53. Kumar, M.; Deka, S. Multiply Twinned AgNi Alloy Nanoparticles as Highly Active Catalyst for Multiple Reduction and Degradation Reactions. *ACS Appl. Mater. Interfaces* **2014**, *6*, 16071–16081. [CrossRef] [PubMed]
54. Saranya, A.; Thamer, A.; Ramar, K.; Priyadharsan, A.; Raj, V.; Murugan, K.; Murad, A.; Maheshwaran, P. Facile One Pot Microwave-Assisted Green Synthesis of Fe_2O_3/Ag Nanocomposites by Phytoreduction: Potential Application as Sunlight-Driven Photocatalyst, Antibacterial and Anticancer Agent. *J. Photochem. Photobiol. B Biol.* **2020**, *207*, 111885. [CrossRef]
55. Abbas, M.; Rao, B.P.; Abdel-Hamed, M.O.; Kim, C. Modified Polyol Route for Synthesis of Fe_3O_4/Ag and α-Fe/Ag Nanocomposite. *J. Alloys Compd.* **2014**, *615*, S308–S312. [CrossRef]
56. Xing, Y.; Bai, X.-H.; Gong, Y.; Peng, M.-L.; Zhang, Y.-Y.; Ma, X.-R.; Zhang, Y. Enhanced Catalytic Properties of Fe_3O_4/Ag Magnetic Microspheres Synthesized by a Novel Thermal Co-Reduction Method. *J. Magn. Magn. Mater.* **2020**, *510*, 166951. [CrossRef]
57. Xing, Y.; Ma, F.F.; Peng, M.L.; Ma, X.R.; Zhang, Y.; Cui, Y.L. Bifunctional Sodium Tartrate as Stabilizer and Reductant for the Facile Synthesis of Fe_3O_4/Ag Nanocomposites with Catalytic Activity. *J. Magn. Magn. Mater.* **2019**, *471*, 133–141. [CrossRef]
58. Bao, Z.Y.; Dai, J.; Lei, D.Y.; Wu, Y. Maximizing Surface-Enhanced Raman Scattering Sensitivity of Surfactant-Free Ag-Fe_3O_4 Nanocomposites through Optimization of Silver Nanoparticle Density and Magnetic Self-Assembly. *J. Appl. Phys.* **2013**, *114*, 124305. [CrossRef]

59. Park, S.B.; White, S.B.; Steadman, C.S.; Pechan, T.; Pechanova, O.; Clemente, H.J.; Thirumalai, R.V.K.G.; Willard, S.T.; Ryan, P.L.; Feugang, J.M. Silver-Coated Magnetic Nanocomposites Induce Growth Inhibition and Protein Changes in Foodborne Bacteria. *Sci. Rep.* **2019**, *9*, 17499. [CrossRef]
60. Chandel, M.; Makkar, P.; Ghosh, N.N. Ag-Ni Nanoparticle Anchored Reduced Graphene Oxide Nanocomposite as Advanced Electrode Material for Supercapacitor Application. *ACS Appl. Electron. Mater.* **2019**, *1*, 1215–1224. [CrossRef]
61. Yan, S.; Sun, D.; Tan, Y.; Xing, X.; Yu, H.; Wu, Z. Synthesis and Formation Mechanism of Ag–Ni Alloy Nanoparticles at Room Temperature. *J. Phys. Chem. Solids* **2016**, *98*, 107–114. [CrossRef]
62. Zhang, C.; Liu, S.; Mao, Z.; Liang, X.; Chen, B. Ag-Ni Core-Shell Nanowires with Superior Electrocatalytic Activity for Alkaline Hydrogen Evolution Reaction. *J. Mater. Chem. A* **2017**, *5*, 16646–16652. [CrossRef]
63. Manoj, K.; Gayathri, S.; Jayabal, P.; Ramakrishnan, V. Synthesis and Characterization of Ni/Ag Nanocomposite for Surface Enhanced Raman Scattering Measurement. *Mater. Res. Express* **2015**, *2*, 65003. [CrossRef]
64. Zhang, Z.; Wang, J.; Chen, C. Near-Infrared Light-Mediated Nanoplatforms for Cancer Thermo-Chemotherapy and Optical Imaging. *Adv. Mater.* **2013**, *25*, 3869–3880. [CrossRef]
65. Dreaden, E.C.; Alkilany, A.M.; Huang, X.; Murphy, C.J.; El-Sayed, M.A. The Golden Age: Gold Nanoparticles for Biomedicine. *Chem. Soc. Rev.* **2012**, *41*, 2740–2779. [CrossRef]
66. Zachanowicz, E.; Kulpa-Greszta, M.; Tomaszewska, A.; Gazińska, M.; Marędziak, M.; Marycz, K.; Pązik, R. Multifunctional properties of binary polyrhodanine manganese ferrite nanohybrids—from the energy converters to biological activity. *Polymers* **2020**, *12*, 2934. [CrossRef]
67. Shipunova, V.O.; Belova, M.M.; Kotelnikova, P.A.; Shilova, O.N.; Mirkasymov, A.B.; Danilova, N.V.; Komedchikova, E.N.; Popovtzer, R.; Deyev, S.M.; Nikitin, M.P. Photothermal Therapy with HER2-Targeted Silver Nanoparticles Leading to Cancer Remission. *Pharmaceutics* **2022**, *14*, 1013. [CrossRef] [PubMed]
68. Furube, A.; Hashimoto, S. Insight into Plasmonic Hot-Electron Transfer and Plasmon Molecular Drive: New Dimensions in Energy Conversion and Nanofabrication. *NPG Asia Mater.* **2017**, *9*, e454. [CrossRef]
69. Guo, J.; Rahme, K.; He, Y.; Li, L.-L.; Holmes, J.D.; O'Driscoll, C.M. Gold Nanoparticles Enlighten the Future of Cancer Theranostics. *Int. J. Nanomed.* **2017**, *12*, 6131. [CrossRef]
70. Jiang, Q.; Zeng, W.; Zhang, C.; Meng, Z.; Wu, J.; Zhu, Q.; Wu, D.; Zhu, H. Broadband Absorption and Enhanced Photothermal Conversion Property of Octopod-like Ag@Ag_2S Core@shell Structures with Gradually Varying Shell Thickness. *Sci. Rep.* **2017**, *7*, 17782. [CrossRef]
71. Qin, Z.; Etheridge, M.; Bischof, J.C. Nanoparticle Heating: Nanoscale to Bulk Effects of Electromagnetically Heated Iron Oxide and Gold for Biomedical Applications. In *Proceedings of the Energy-based Treatment of Tissue and Assessment VI*; Ryan, T.P., Ed.; SPIE: Bellingham, WA, USA, 2011; Volume 7901, p. 79010C.
72. Boldoo, T.; Ham, J.; Kim, E.; Cho, H. Review of the Photothermal Energy Conversion Performance of Nanofluids, Their Applications, and Recent Advances. *Energies* **2020**, *13*, 5748. [CrossRef]
73. Hu, R.; Zheng, M.; Wu, J.; Li, C.; Shen, D.; Yang, D.; Li, L.; Ge, M.; Chang, Z.; Dong, W. Core-Shell Magnetic Gold Nanoparticles for Magnetic Field-Enhanced Radio-Photothermal Therapy in Cervical Cancer. *Nanomaterials* **2017**, *7*, 111. [CrossRef]
74. Xu, X.; Liu, X.; Tan, L.; Cui, Z.; Yang, X.; Zhu, S.; Li, Z.; Yuan, X.; Zheng, Y.; Yeung, K.W.K.; et al. Controlled-Temperature Photothermal and Oxidative Bacteria Killing and Acceleration of Wound Healing by Polydopamine-Assisted Au-Hydroxyapatite Nanorods. *Acta Biomater.* **2018**, *77*, 352–364. [CrossRef] [PubMed]
75. Hernández, Y.; Galarreta, B.C. Noble Metal-Based Plasmonic Nanoparticles for SERS Imaging and Photothermal Therapy. In *Nanomaterials for Magnetic and Optical Hyperthermia Applications*; Elsevier: Amsterdam, The Netherlands, 2018; pp. 83–109, ISBN 9780128139295.
76. Kaur, P.; Aliru, M.L.; Chadha, A.S.; Asea, A.; Krishnan, S. Hyperthermia Using Nanoparticles-Promises and Pitfalls. *Int. J. Hyperth.* **2016**, *32*, 76–88. [CrossRef] [PubMed]
77. Petryayeva, E.; Krull, U.J. Localized Surface Plasmon Resonance: Nanostructures, Bioassays and Biosensing-A Review. *Anal. Chim. Acta* **2011**, *706*, 8–24. [CrossRef]
78. Oldenburg, S.J.; Averitt, R.D.; Westcott, S.L.; Halas, N.J. Nanoengineering of Optical Resonances. *Chem. Phys. Lett.* **1998**, *288*, 243–247. [CrossRef]
79. Justin, C.; Philip, S.A.; Samrot, A.V. Synthesis and Characterization of Superparamagnetic Iron-Oxide Nanoparticles (SPIONs) and Utilization of SPIONs in X-ray Imaging. *Appl. Nanosci.* **2017**, *7*, 463–475. [CrossRef]
80. Wu, M.; Huang, S. Magnetic Nanoparticles in Cancer Diagnosis, Drug Delivery and Treatment. *Mol. Clin. Oncol.* **2017**, *7*, 738–746. [CrossRef] [PubMed]
81. Zhao, J.; Zhou, C.; Li, M.; Li, J.; Li, G.; Ma, D.; Li, Z.; Zou, D. Bottom-up Synthesis of Ultra-Small Molybdenum Disulfide-polyvinylpyrrolidone Nanosheets for Imaging-Guided Tumor Regression. *Oncotarget* **2017**, *8*, 106707–106720. [CrossRef]
82. Wang, Z.; Li, S.; Zhang, M.; Ma, Y.; Liu, Y.; Gao, W.; Zhang, J.; Gu, Y. Laser-Triggered Small Interfering RNA Releasing Gold Nanoshells against Heat Shock Protein for Sensitized Photothermal Therapy. *Adv. Sci.* **2017**, *4*, 1600327. [CrossRef] [PubMed]

83. Wo, F.; Xu, R.; Shao, Y.; Zhang, Z.; Chu, M.; Shi, D.; Liu, S. A Multimodal System with Synergistic Effects of Magneto-Mechanical, Photothermal, Photodynamic and Chemo Therapies of Cancer in Graphene-Quantum Dot-Coated Hollow Magnetic Nanospheres. *Theranostics* **2016**, *6*, 485–500. [CrossRef] [PubMed]
84. Mehrali, M.; Ghatkesar, M.K.; Pecnik, R. Full-Spectrum Volumetric Solar Thermal Conversion via Graphene/Silver Hybrid Plasmonic Nanofluids. *Appl. Energy* **2018**, *224*, 103–115. [CrossRef]